Geophysical Research Letters

RESEARCH LETTER
10.1029/2024GL108923

Tidal Control of Equatorial Vertical E × B Drift Under Solar Minimum Conditions

H.-L. Liu[1] and **A. Maute**[2]

[1]High Altitude Observatory, National Center for Atmospheric Research, Boulder, CO, USA, [2]CIRES, NOAA Space Weather Prediction Center, University of Colorado Boulder, Boulder, CO, USA

Abstract Observations show that equatorial ionospheric vertical drifts during solar minimum differ from the climatology between late afternoon and midnight. By analyzing WACCM-X simulations, which reproduce this solar cycle dependence, we show that the interplay of the dominant migrating tides, their propagating and in situ forced components, and their solar cycle dependence impact the F-region wind dynamo. In particular, the amplitude and phase of the propagating migrating semidiurnal tide (SW2) in the F-region plays a key role. Under solar minimum conditions, the SW2 tide propagate to and beyond the F-region in the winter hemisphere, and consequently its zonal wind amplitude in the F-region is much stronger than that under solar maximum conditions. Furthermore, its phase shift leads to a strong eastward wind perturbation near local midnight. This in turn drives a F-region dynamo with an equatorial upward drift between 18 and 1 hr local times.

Plain Language Summary The vertical ion motion in the equatorial ionosphere plays a key role in the space weather. Satellite observations found that such vertical motion during periods with low solar activity can be quite different from the known climatology, and the cause is not clear. Using a whole atmosphere general circulation model, WACCM-X, we are able to reproduce the pattern of the vertical ion motion similar to that observed during low activity solar cycle periods. By analyzing the model results, we find that the relative significance of the different atmosphere tidal wave components and its variation with solar activity contribute to the solar dependence of the vertical ion motion. The propagating altitudes of tide with 12-hr period, as well as where and when the tidal wind becomes large, are of particular importance.

Key Points:

- Upward equatorial vertical ion drift near midnight under solar minimum conditions reproduced by WACCM-X
- Modulation of F-region dynamo by propagating semidiurnal tide is much stronger during solar minimum
- Tidal phase change in equatorial F-region during solar minimum shifts upward drift toward midnight

Supporting Information:

Supporting Information may be found in the online version of this article.

Correspondence to:

H.-L. Liu,
liuh@ucar.edu

Citation:

Liu, H.-L., & Maute, A. (2024). Tidal control of equatorial vertical E × B drift under solar minimum conditions. *Geophysical Research Letters*, *51*, e2024GL108923. https://doi.org/10.1029/2024GL108923

Received 22 FEB 2024
Accepted 14 MAY 2024

Author Contributions:

Conceptualization: H.-L. Liu
Data curation: H.-L. Liu
Formal analysis: H.-L. Liu
Funding acquisition: H.-L. Liu, A. Maute
Investigation: H.-L. Liu, A. Maute
Methodology: H.-L. Liu, A. Maute
Project administration: H.-L. Liu
Resources: H.-L. Liu
Software: H.-L. Liu, A. Maute
Supervision: H.-L. Liu
Validation: H.-L. Liu
Visualization: H.-L. Liu
Writing – original draft: H.-L. Liu, A. Maute
Writing – review & editing: H.-L. Liu, A. Maute

1. Introduction

The ionospheric E × B drift is a key quantity in ionospheric electrodynamics. In particular, the vertical component of E × B drift at dusk and during night time can play a key role in the onset of F-region irregularities (Anderson et al., 2004; Fejer et al., 1999; Huang, 2018; Huang & Hairston, 2015; Kil et al., 2009). The vertical E × B drift climatology, based on radar and satellite measurements, shows a clear seasonal variation and solar activity dependence (Scherliess & Fejer, 1999). The most significant variability is found in the vertical drift around dusk: strong pre-reversal enhancement (PRE) of the vertical drift often occurs around equinox and under more active solar conditions. The E and F regions dynamo and the alignment of the geomagnetic field lines and the evening terminator are thought to be responsible for the PRE and its seasonal and solar activity dependence (Abdu et al., 1981; Farley et al., 1986; Tsunoda, 1985). Fesen et al. (2000) simulated PRE and its seasonal and solar activity dependence using the Thermosphere/Ionosphere/Electrodynamic General Circulation Model, and found that the E-region migrating semidiurnal tide (SW2) plays an important role. The seasonal and solar activity dependence of PRE is recently simulated by the Whole Atmosphere Community Climate Model with thermosphere/ionosphere extension (WACCM-X) (Liu et al., 2018). The analysis of WACCM-X simulation under solar maximum conditions found that the pattern of longitudinal-seasonal variation of PRE displays a remarkable similarity to the pattern of the equatorial plasma bubble occurrence rate (Liu, 2020). Moreover, the simulated PRE shows large day-to-day variability, and it is strongly influenced by the variability of both migrating and non-migrating tides.

Vertical E × B drifts measured by the Coupled Ion Neutral Dynamics Investigation Ion Velocity Meter instrument onboard the Communication/Navigation Outage Forecasting System (C/NOFS), on the other hand, have notable differences from the aforementioned climatology at solstices under solar minimum conditions (Stoneback et al., 2011): in contrast to the climatological behavior of upward drifts during the day and downward drifts at night (with weak or no PRE in between), downward drifts in the afternoon and upward drifts near midnight are

observed. The upward drifts at night correspond to regions with a high occurrence of post-midnight irregularities during the December 2008 and June 2009 solstices. The apparent semidiurnal signal was postulated to be related to the semidiurnal tides in the E-region. It is well established that both migrating and non-migrating tides play important roles in ionospheric electrodynamics (e.g., Fesen et al., 2000; Hagan et al., 2007; Forbes et al., 2008; England, 2012, and references therein). It is unclear, however, with semidiurnal tides being present at all seasons and under all solar conditions why this semidiurnal signature only becomes apparent around solstice especially during northern summer under solar minimum conditions.

In this study, we will investigate the possible mechanisms that cause upward drift near midnight, and the processes that control the seasonal and solar cycle variation of the vertical E × B drifts using WACCM-X simulations, which reproduce salient features of the variation. Further, an ionospheric electric dynamo model is used to delineate the roles of E and F-region dynamo. A description of the models is given in Section 2. Analysis of model results is presented in Section 3, followed by Conclusions (Section 4).

2. Model Description

WACCM-X is one of the atmosphere components of the NCAR Community Earth System Model (CESM) (Hurrell et al., 2013) (also http://www.cesm.ucar.edu/ for information on the most recent version, CESM version 2), with its top boundary set at the upper thermosphere. Detailed descriptions of the thermospheric and ionospheric physics used in the model can be found in Liu et al. (2010, 2018). The model configuration used in this study is the same as that described by Liu (2020), except that solar minimum condition is used here with the solar radio flux at 10.7 cm (F10.7 flux) set at 70 solar flux unit (sfu, 10^{-22} W m^{-2} Hz^{-1}). It is a free running climate simulation over three model year under the same solar minimum conditions.

The stand-alone ionospheric electrodynamo introduced by Maute and Richmond (2017) is employed. In the current study, we consider only forcing by the wind dynamo, which are provided by WACCM-X together with the ionospheric conductivities. Compared to the electrodynamo in WACCM-X, the stand-alone dynamo considers the flux tube geometry with the full 3D variation of apex quantities, however the effect on the electric potential solution is small and therefore the E × B drift from the stand-alone electrodynamo can be compared to the WACCM-X E × B drift.

3. Results

From WACCM-X simulations, it is seen that the equatorial vertical E × B drift ($(E \times B)_z$, referred to as vertical drift hereafter) in June under solar minimum (referred to as J_{min} hereafter) conditions display local time (LT)/longitudinal dependence that is different from those in June/solar maximum (J_{max}) and December solar maximum (D_{max}) and solar minimum (D_{min}) (Figure 1). For the specific universal time shown here (UT 20 hr), the J_{min} vertical drift becomes downward between 16 and 20 LT (with the largest downward drift of over 20 m s^{-1} between 18 and 19 hr LT/15–30°W), and upward between 20 LT and midnight (with peak value of 20 m s^{-1} at ∼22 LT/30°E) (Figure 1a). In contrast, the vertical drifts in all the other panels show the typical PRE at 20 LT or earlier, followed by a rapid reversal to downward afterward (before 23 hr LT). In the afternoon sector (14–16 hr LT/90–60°W) the equatorial vertical drift in J_{min} is upward, switching quickly to downward afterward. The afternoon equatorial vertical drifts in the other three cases, on the other hand, are weakly upward, straddling upward peaks before and after. Therefore, the equatorial vertical drift for J_{min} displays a strong semidiurnal signature, with peak values between 15 and 25 m s^{-1} at ∼10 and 22 LT (upward) and ∼18:30 and 5 LT (downward). In the other cases, the upward peaks in the morning and around dusk (PRE) are both prominent, but the downward drift in the afternoon is either very weak or non-existing.

The model results, including the vertical drift, show large day-to-day variability (Liu, 2020), and the LT/UT and longitude dependence shown in Figure 1 may not be the same on different days. To determine how robust this feature is, we further examine the monthly climatology of the vertical drift under solar minimum conditions. Figure 2a is the vertical drift as a function of longitude and LT obtained by averaging over June of the three model years. The semidiurnal structure is clearly seen in the plot at most longitudes, with LT dependence similar to that from Figure 1a. Moreover, the longitudinal variation is evident in the monthly plot. The specific structure of the longitude variation agrees with the C/NOFS results (June 2009) (Stoneback et al., 2011, Figure 7) in some longitude sectors, but not in others. The downward drift between 16 and 20 LT is rather strong between 30°E and 130°E and 0°W–30°W and near 0 in the Pacific and American sectors (180°W–70°W). These are in general

10.1029/2024GL108923

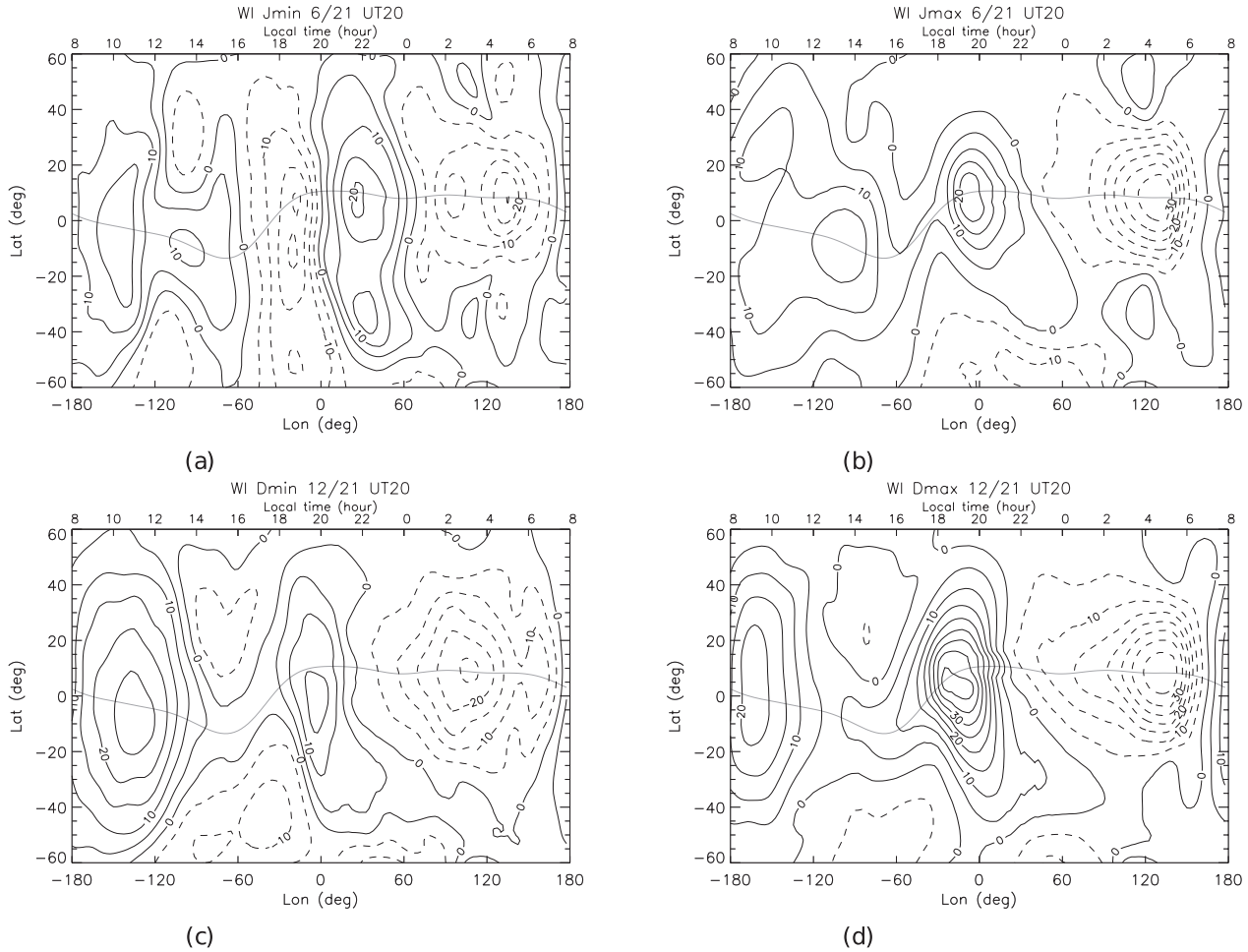

Figure 1. The vertical E × B drift (WI in figure) on day 21 of June (a, b) and day 21 of December (c, d) at 20 hr UT under solar minimum (a, c) and solar maximum (b, d) conditions. The local times are marked on the upper *x* axis. Contour interval: 5 m s^{-1} (solid: upward). Thin gray line: The magnetic equator.

agreement with the C/NOFS results. It then turns upward at most longitudes except between 70°E and 110°E (remaining downward) and 150°W–120°W (near 0 LT). By midnight, the vertical drift becomes 0 or downward at most longitudes except between 30°E and 65°E. This upward drift around midnight is comparable to that in C/NOFS. The monthly average of the vertical drift at local midnight is shown in Figure 2b for the whole simulation

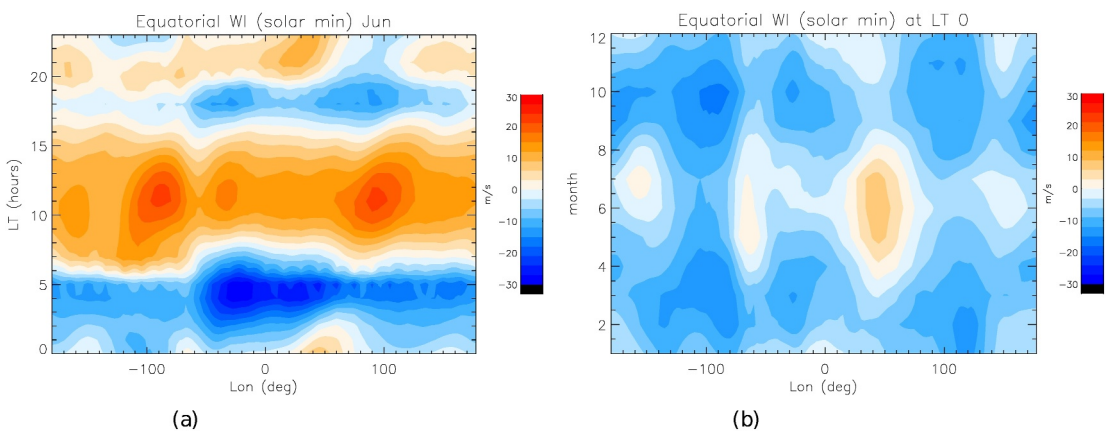

Figure 2. Monthly averaged vertical E × B drift (a) for June over all local times (LTs), and (b) for 0 hr LT over all year under solar minimum conditions.

year under solar minimum conditions. It is seen that at midnight the average vertical drift is upward only during northern summer months (May-July) between 30°E and 65°E. Three other local maxima are seen at 150°E, 150°W, and 65°W, with drift values of −3 m s^{-1}, 0 and 0, respectively. This four peak structure results from modulation of the dynamo by non-migrating tides diurnal eastward propagating wavenumber 3 (DE3), as determined from a spectral decomposition calculation (Figure S1 in Supporting Information S1). During northern winter, the monthly average of the vertical drift at midnight is weakly downward with longitudinal variation somewhat similar to that during northern summer. It is also noted that although on individual days the vertical drifts at midnight generally follow similar longitudinal patterns as the monthly averages, they can be upward at multiple longitude locations under solar minimum conditions for both June and December (Figure S2 in Supporting Information S1).

The semidiurnal signature of the equatorial vertical drift during northern summer under solar minimum conditions has been identified by Stoneback et al. (2011) from C/NOFS observations. The simulation results discussed above for J_{min}, including the LT variation with longitudes, compare quite well with the C/NOFS results. As suggested by Stoneback et al. (2011), this semidiurnal variation is probably related to semidiurnal tides in the E-region. Since this feature is reproduced in WACCM-X simulations, we will analyze the model results to understand the connection, especially regarding to the cause of the variation with season and solar activities.

Here we focus on the E to F-region dynamo, in particular the effects of the neutral winds. Specifically, electric field and E × B drifts are calculated using the standalone electrodynamo model with neutral winds and ionospheric conductivities input from WACCM-X. UT 20 hr is chosen for detailed analysis because this is within the time period when the equatorial vertical drift near midnight displays the largest upward values (between 30 and 65°E) as discussed above and seen in Figures 1 and 2. In Figure 3 the solid lines are equatorial vertical drifts obtained from the standalone electrodynamo model with WACCM-X input. In the control experiments, only neutral winds in one altitude region are used while winds at other altitudes are set to 0 in order to determine their respective contributions to the vertical drifts. Specifically, three altitude regions between 10^{-7}, 1.2×10^{-6}, 1.5×10^{-5}, and 8.5×10^{-5} hPa (approximately 250/175/125/105 km, respectively, for solar minimum, and 330/210/130/105 km, respectively, for solar maximum) are examined. These regions correspond to F-region, upper E-region where SW2 peaks in the winter hemisphere, and lower E-region where SW2 peaks in the summer hemisphere (Figure 4), and the dotted, dashed and dash-dot lines correspond to the equatorial vertical drifts driven by the wind dynamo in these regions, respectively. The plotting ranges are different for each of the sub-figures for better visualization of the longitude/LT dependence. It is seen that the solid lines indeed reproduce the vertical drifts from WACCM-X, with the nighttime upward equatorial drift for J_{min} peaking at much later times (near 22 LT) than those in the J_{max} and D_{min} cases (near 19 LT). The drifts produced by the dynamo processes of the three regions do not add up to the total drift, since contributions above 10^{-7} hPa or below 8.5×10^{-5} are not accounted for. This decomposition confirms the dominant role of E-region dynamo during the day and F-region dynamo during the night. In all three cases, the vertical drifts by the lower E-region dynamo are qualitatively similar: they have an upward peak in the morning/noon sector, and become downward between ∼16 LT and midnight with the largest values between ∼18–20 LT. This variation is consistent with a previous analysis of WACCM-X drift results around dusk (Liu, 2020). Quantitatively, the largest change from the upward drift in the morning to the downward drift near dusk is found in J_{min}. The upward drift from E-region dynamo in J_{min} also peaks earlier (before 10 hr LT) than the other two cases.

The vertical drift by the F-region dynamo for J_{min}, on the other hand, behaves differently from the other two cases: the upward drift peaks at ∼21:30 LT and remains upward till after local midnight, while in the other two cases the upward drifts peak at 19 LT, and become downward at 22–23 LT. Before dusk (16–19 LT), the vertical drift from the F-region dynamo also shows difference between J_{min} and the other two: it remains near zero in J_{min} but is upward and becomes larger toward dusk in J_{max}/D_{min}. Since the downward drift peaks due to E-region dynamo are between 18 and 20 hr LT, the near zero vertical drift before dusk and upward drift peak at later LT in J_{min} result in a prominent downward drift before 20 hr LT, followed by a large upward peak near 22 hr LT. In the other two cases, the peak downward and upward drifts occur at similar LTs and thus offset each other. It is also seen that the upper E-region contributes to the dynamo similarly to the lower E-region before dusk and to the F-region after, though with smaller magnitudes. We also note that DE3 peaks in the upper E region, and it is responsible for the spatial modulation as seen in Figure 2b. The total vertical drift in the J_{min} case therefore shows an apparent semidiurnal feature, with two large upward peaks and two large downward peaks, similar to the observations as reported in Stoneback et al. (2011).

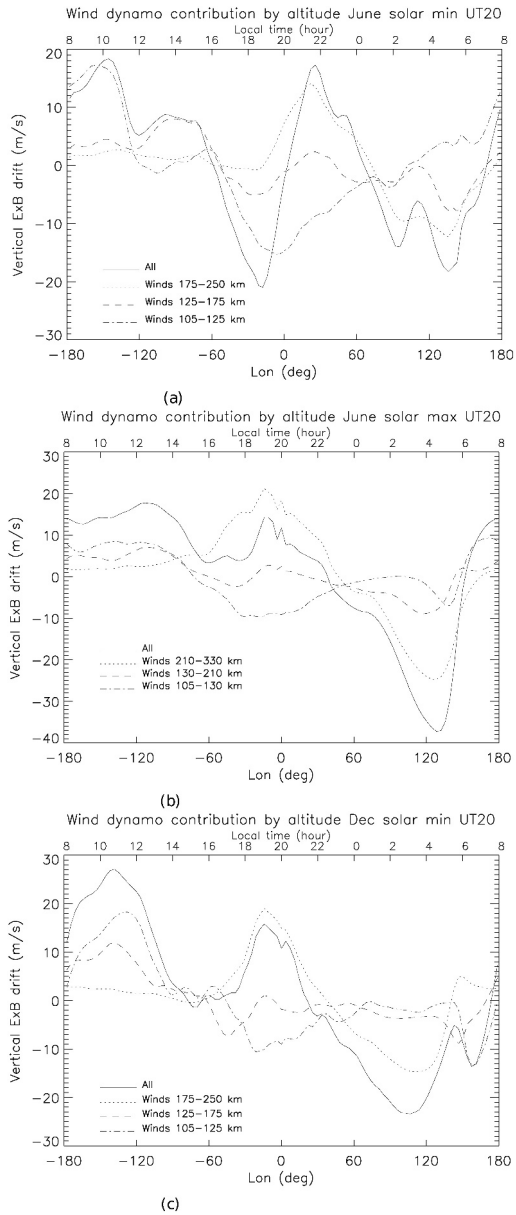

Figure 3. Contribution to total equatorial vertical E × B drift by different altitude regions for (a) June, solar minimum, (b) June, solar maximum and (c) December, solar minimum. 20 hour UT is shown, and the local times are marked by the upper *x*-axis.

The seasonal variation and solar cycle dependence of the leading tidal modes, SW2 and the diurnal migrating tide (DW1), are then examined. By comparing the zonal wind component of SW2 at F-region height (5.7×10^{-7} hPa) (Figures 4a and 4b), it is seen that SW2 attains maximum values (~40 m s^{-1}) between June and August (JJA) under solar minimum conditions. The wave amplitude is the largest in the southern hemisphere, but even in the northern hemisphere it is over 20 m s^{-1}. In contrast, the peak SW2 amplitude during JJA under solar maximum conditions is less than 20 m s^{-1}, and at equatorial latitudes the amplitude is less than 10 m s^{-1}. The SW2 phase (calculated at the equator) during JJA under solar minimum conditions approaches 12 hr LT, and the eastward wind perturbations are thus strongest approaching noon and midnight. The SW2 phase during JJA under solar maximum conditions, on the other hand, is between 6–7 and 18–19 hr LT–almost 180° out of phase with that under solar minimum condition. It would be at its strongest westward phase near midnight. It is noted that under solar minimum conditions the SW2 phase also approaches 12 LT during northern winter months, but the wave amplitude is weaker than during northern summer.

DW1 zonal wind component in the F-region also shows different seasonal features under different solar conditions (Figures 4c and 4d). Under solar minimum conditions, the DW1 wave amplitude (~40 m s^{-1}) at equatorial latitudes is weak in comparison to mid-high latitudes in the summer hemisphere. This is the opposite under solar maximum conditions, when the DW1 amplitude is the largest at equatorial latitudes. The DW1 phase in the equatorial F-region is stable, with that under solar minimum conditions slightly later (22 hr LT) than that under solar maximum conditions (21 hr LT). Therefore, under solar minimum conditions the zonal wind perturbations of SW2 and DW1 are comparable at equatorial to mid-latitudes, and their superposition results in an enhanced eastward wind perturbation near local midnight in the F-region. This is directly responsible for driving the extended upward E × B drift seen in Figure 3a for J_{min}. The SW2 tide does not significantly reinforce the eastward wind in the equatorial F-region in other season or under more active solar conditions, because its zonal wind perturbation is weaker and/or its phase is opposite (westward) near midnight.

To better understand the solar activity dependence of the tidal waves, the latitude/height structure of the amplitudes and phases of SW2 and DW1 for J_{min} and J_{max} are examined in Figures 4e–4h. Figures 4e and 4f also show the F, upper and lower E regions for the dynamo analysis presented above, as well as vertical profiles of Pedersen conductivity that help guide this decomposition. It is clear that these tides transition from propagating modes to in-situ forced/trapped modes with increasing altitudes. For the J_{min} SW2, it shows phase propagation above ~330 km (~10^{-8} hPa) over the southern (winter) hemisphere and northern equatorial latitudes, while J_{max} SW2 phase stagnates at ~300 km (2×10^{-7} hPa). Consequently, the SW2 amplitude at the F-region altitudes is much larger in the case of J_{min} as seen in Figure 4. The phase progression of DW1 in J_{min} also extends to higher altitudes (~250 km, 10^{-7} hPa) than J_{max} (~220 km, 10^{-6} hPa), but the F-region wind is generally dominated by the in situ forced DW1 winds, especially at the equator and summer high latitudes under solar maximum conditions (also seen in Figure 4). It is therefore evident that SW2 can significantly modulate the F-region wind under solar minimum conditions, but not so much under solar maximum conditions. This is also clearly seen from the total zonal wind at the equator (Figure S3 in Supporting Information S1).

4. Conclusions

Our analysis suggests that the E-region wind dynamo have similar contributions under different solar cycle conditions, and the interplay of the dominant migrating tides, DW1 and SW2, determines the F-region wind

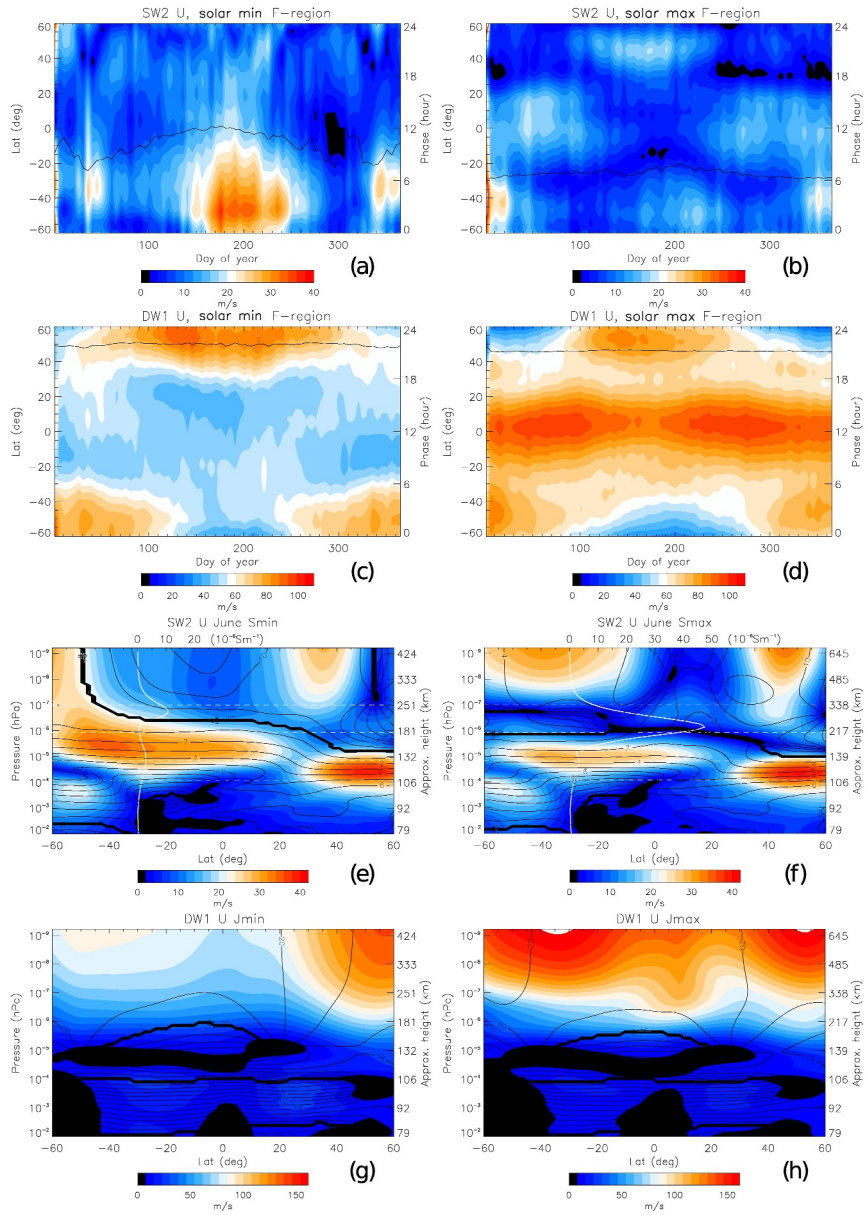

Figure 4. Seasonal variation of SW2 zonal wind amplitude (U, color contour) and phase (black line) in the F-region (5.7×10^{-7} hPa) for (a) solar minimum and (b) solar maximum. (c, d) Similar to panels (a, b) but for DW1. In panels (a–d) the phase values (marked by the *y*-axis on the right side) are in terms of local times for the respective tidal components at the equator. The latitude-height structure of the amplitude (color contour) and phase (line contour) of SW2 zonal wind for June under (e) solar minimum and (f) solar maximum conditions. (g, h) Similar to panels (e, f) but for DW1. The contour line interval is 1 hr in (e, f) and 2 hr in (g, h). The vertical profiles of Pedersen conductivity at 30°S are plotted in (e) (solar minimum) and (f) (solar maximum), and the conductivity values can be read from the upper *x*-axis (unit: 10^{-6} S m^{-1}). The horizontal dashed lines are at 10^{-7} hPa, 1.2×10^{-6}, 1.5×10^{-5}, and 8.5×10^{-5} hPa pressure levels.

dynamo and the solar cycle variation of the equatorial E × B drift. Under solar minimum conditions, the SW2 tide propagate to and beyond the F-region in the winter hemisphere, and consequently its zonal wind amplitude in the F-region is much stronger than that under solar maximum conditions. The zonal wind DW1 in the F-region, on the other hand, comes mostly from in-situ forcing under both solar maximum and minimum conditions, but with much larger amplitude at low latitudes for the former. Consequently, the SW2 tidal modulation of the F-region wind is more significant under solar minimum conditions. Moreover, the SW2 zonal wind phase at F-region height also shows a solar cycle dependence: ∼12 LT during solar minimum and ∼6 LT during solar

maximum. The superposition of DW1 and SW2 results in a strong eastward wind perturbation near local midnight, and a westward (or weakly eastward) wind around dusk in the F-region under solar minimum conditions. This in turn drives a F-region dynamo with an equatorial upward drift between 18 and 01 hr LT, reaching its maximum near 22 hr LT. In contrast, the F-region wind is dominated by DW1 during solar maximum (eastward between 16 and 4 hr LT), and the SW2 modulation is rather insignificant. This drives an equatorial upward drift within the LT range 07–23 hr LT, with peak values near 19 hr. The total equatorial vertical E × B drift during solar minimum is downward in the local afternoon and dusk, followed by an upward drift that extends toward midnight. Therefore, the apparent semidiurnal variation during solar minimum is not a direct manifestation of SW2 in the E-region: The upward peaks in the local morning and pre-midnight are driven mainly by the E-region wind and the F-region wind respectively, and the downward peaks near the dusk peak and post midnight/early morning are by E-region and F-region winds, respectively.

Longitudinal variation is apparent in both observations (Stoneback et al., 2011) and modeling results presented here. The four-peak structure as seen in Figure 2 suggests the modulation by non-migrating tides, which is known to cause longitudinal variation (e.g., Fang et al., 2013). However, it is unclear why the magnitudes of the four peaks differ, with the strongest midnight upward drift at 30°E–65°E during northern summer months. Modulation by the geometry and strength of geomagnetic field is another cause of longitudinal variation (e.g., Fang et al., 2012). The detailed mechanism responsible for the longitudinal variation of the nighttime vertical drift, including the upward drift at midnight at specific longitude sectors, needs to be further elucidated in future studies. Moreover, there is an apparent difference between the equatorial upward drift at June and December solstices under solar minimum conditions, with the semidiurnal feature and the upward drift around midnight more pronounced in the former case. In the model, this difference stems from the different semidiurnal tidal winds at the F-region height, with the winter hemisphere wave amplitude much stronger around June solstice. The cause of this hemispheric difference in SW2 in the thermosphere should be further examined in future studies.

Data Availability Statement

Data: The model output used for this study is available through GLOBUS (Liu & Maute, 2024a). Registration for a free Globus account is required.

Software: The simulations are based on NCAR CESM WACCM-X development tag 6_1_023 (Liu & Maute, 2024b).

Acknowledgments
HLL acknowledges partial support by NASA Grants 80NSSC20K1323, 80NSSC20K0601, 80NSSC20K0633, 80NSSC21K1305, 80NSSC20K0189, 80NSSC22K1018, 80NSSC22M0163, 80NSSC23K1237, and 80NSSC24K0195. AM is supported by NASA awards 80NSSC23K1123, 80NSSC20K1784, and 80MSFC20D0004. National Center for Atmospheric Research is a major facility sponsored by the National Science Foundation under Cooperative Agreement No. 1852977.

References

Abdu, M. A., Bittencourt, J. A., & Batista, I. S. (1981). Magnetic declination control of the equatorial F region dynamo electric field development and spread F. *Journal of Geophysical Research*, *86*(A13), 11443–11446. https://doi.org/10.1029/JA086iA13p11443

Anderson, D. N., Reinisch, B., Valladares, C. E., Chau, J., & Veliz, O. (2004). Forecasting the occurrence of ionospheric scintillation activity in the equatorial ionosphere on day-to-day basis. *Journal of Atmospheric and Solar-Terrestrial Physics*, *66*(17), 1567–1572. https://doi.org/10.1016/j.jastp.2004.07.010

England, S. L. (2012). A review of the effects of non-migrating atmospheric tides on the earth's low-latitude ionosphere. *Space Science Reviews*, *168*(1–4), 211–236. https://doi.org/10.1007/s11214-011-9842-4

Fang, T.-W., Akmaev, R., Fuller-Rowell, T., Wu, F., Maruyama, N., & Millward, G. (2013). Longitudinal and day-to-day variability in the ionosphere from lower atmosphere tidal forcing. *Geophysical Research Letters*, *40*(11), 2523–2528. https://doi.org/10.1002/grl.50550

Fang, T.-W., Fuller-Rowell, T., Akmaev, R., Wu, F., Wang, H., & Anderson, D. (2012). Longitudinal variation of ionospheric vertical drifts during the 2009 sudden stratospheric warming. *Journal of Geophysical Research*, *117*(A3), A03324. https://doi.org/10.1029/2011JA017348

Farley, D. T., Bonelli, E., Fejer, B. G., & Larsen, M. F. (1986). The prereversal enhancement of the zonal electric field in the equatorial ionosphere. *Journal of Geophysical Research*, *91*(A12), 13723–13728. https://doi.org/10.1029/ja091ia12p13723

Fejer, B. G., Scherliess, L., & de Paula, E. R. (1999). Effects of the vertical plasma drift velocity on the generation and evolution of equatorial spread F. *Journal of Geophysical Research*, *104*(A9), 19859–19869. https://doi.org/10.1029/1999ja900271

Fesen, C. G., Crowley, G., Roble, R. G., Richmond, A. D., & Fejer, B. G. (2000). Simulation of the pre-reversal enhancement in the low latitude vertical ion drift. *Geophysical Research Letters*, *27*(13), 1851–1854. https://doi.org/10.1029/2000gl000061

Forbes, J. M., Zhang, X., Palo, S., Russell, J., Mertens, C. J., & Mlynczak, M. (2008). Tidal variability in the ionospheric dynamo region. *Journal of Geophysical Research*, *113*(A2), 1062. https://doi.org/10.1029/2007JA012737

Hagan, M. E., Maute, A., Roble, R. G., Richmond, A. D., Immel, T. J., & England, S. L. (2007). Connections between deep tropical clouds and the Earth's ionosphere. *Geophysical Research Letters*, *34*(20), L20109. https://doi.org/10.1029/2007GL030142

Huang, C.-S. (2018). Effects of the postsunset vertical plasma drift on the generation of equatorial spread F. *Progress in Earth and Planetary Science*, *5*(1), 3. https://doi.org/10.1186/s40645-017-0155-4

Huang, C.-S., & Hairston, M. R. (2015). The postsunset vertical plasma drift and its effects on the generation of equatorial plasma bubbles observed by the C/NOFS satellite. *Journal of Geophysical Research: Space Physics*, *120*(3), 2263–2275. https://doi.org/10.1002/2014JA020735

Hurrell, J. W., Holland, M. M., Gent, P. R., Ghan, S., Kay, J. E., Kushner, P. J., et al. (2013). The community earth system model: A framework for collaborative research. *Bulletin of the American Meteorological Society*, *94*(9), 1339–1360. https://doi.org/10.1175/BAMS-D-12-00121.1

Kil, H., Paxton, L. J., & Oh, S.-J. (2009). Global bubble distribution seen from ROCSAT-1 and its association with the evening prereversal enhancement. *Journal of Geophysical Research*, *114*(A6), A06307. https://doi.org/10.1029/2008JA013672

Liu, H.-L. (2020). Day-to-day variability of pre-reversal enhancement in the vertical ion drift in response to large-scale forcing from the lower atmosphere. *Space Weather*, *18*(4), e2019SW002334. https://doi.org/10.1029/2019SW002334

Liu, H.-L., Bardeen, C. G., Foster, B. T., Lauritzen, P., Liu, J., Lu, G., et al. (2018). Development and validation of the whole atmosphere community climate model with thermosphere and ionosphere extension (WACCM-X 2.0). *Journal of Advances in Modeling Earth Systems*, *10*(2), 381–402. https://doi.org/10.1002/2017MS001232

Liu, H.-L., Foster, B. T., Hagan, M. E., McInerney, J. M., Maute, A., Qian, L., et al. (2010). Thermosphere extension of the whole atmosphere community climate model. *Journal of Geophysical Research*, *115*(A12), A12302. https://doi.org/10.1029/2010JA015586

Liu, H.-L., & Maute, A. (2024a). Model output used for "Tidal control of equatorial vertical E × B drift under solar minimum conditions" [Dataset]. *TinyURL*. Retrieved from https://tinyurl.com/mv2e6e2u

Liu, H.-L., & Maute, A. (2024b). Model used for "Tidal control of equatorial vertical E × B drift under solar minimum conditions" [Software]. *Zenodo*. https://doi.org/10.5281/zenodo.10982787

Maute, A., & Richmond, A. (2017). F-region dynamo simulations at low and mid-latitude. *Space Science Reviews*, *206*(1–4), 471–493. https://doi.org/10.1007/s11214-016-0262-3

Scherliess, L., & Fejer, B. G. (1999). Radar and satellite global equatorial F region vertical drift model. *Journal of Geophysical Research*, *104*(A4), 6829–6842. https://doi.org/10.1029/1999ja900025

Stoneback, R. A., Heelis, R. A., Burrell, A. G., Coley, W. R., Fejer, B. G., & Pacheco, E. (2011). Observations of quiet time vertical ion drift in the equatorial ionosphere during the solar minimum period of 2009. *Journal of Geophysical Research*, *116*(A12), 1434. https://doi.org/10.1029/2011JA016712

Tsunoda, R. T. (1985). Control of the seasonal and longitudinal occurrence of equatorial scintillations by the longitudinal gradient in integrated E region Pedersen conductivity. *Journal of Geophysical Research*, *90*(A1), 447–456. https://doi.org/10.1029/ja090ia01p00447